First detection of silicon-bearing molecules in η Car

C. Bordiu ,[1] J. R. Rizzo ,[2,3] F. Bufano ,[1] G. Quintana-Lacaci ,[4] C. Buemi ,[1] P. Leto ,[1]
F. Cavallaro ,[1] L. Cerrigone,[5] A. Ingallinera ,[1] S. Loru,[1] S. Riggi ,[1] C. Trigilio,[1] G. Umana ,[1] and
E. Sciacca [1]

[1]*INAF-Osservatorio Astrofisico di Catania, Via Santa Sofia 78, 95123 Catania*
[2]*Centro de Astrobiología (INTA-CSIC), Ctra. M-108, km. 4, E-28850 Torrejón de Ardoz, Madrid, Spain*
[3]*ISDEFE, Beatriz de Bobadilla 3, E-28040 Madrid, Spain*
[4]*Group of Molecular Astrophysics. IFF. CSIC. C/ Serrano 123, E-28006, Madrid, Spain*
[5]*Joint ALMA Observatory, Alonso de Córdova 3107, Vitacura, 8320000, Santiago, Chile*

ABSTRACT

We present ALMA band 6 observations of the luminous blue variable η Car, obtained within the ALMAGAL program. We report SiO $J = 5 \to 4$, SiS $J = 12 \to 11$ and SiN $N = 5 \to 4$ emission in the equatorial region of the Homunculus nebula, constituting the first detection of silicon- and sulphur-bearing molecules in the outskirts of a highly evolved, early-type massive star. SiO, SiS and SiN trace a clumpy equatorial ring that surrounds the central binary at a projected distance of ~ 2 arcsec, delineating the inner rims of the butterfly-shaped dusty region. The formation of silicon-bearing compounds is presumably related to the continuous recycling of dust due to the variable wind regime of η Car, that destroys grains and releases silicon back to gas phase. We discuss possible formation routes for the observed species, contextualizing them within the current molecular inventory of η Car. We find that the SiO and SiS fractional abundances in localised clumps of the ring, 6.7×10^{-9} and 1.2×10^{-8} respectively, are exceptionally lower than those measured in C- and O-rich AGB stars and cool supergiants; while the higher SiN abundance, 3.6×10^{-8}, evidences the nitrogen-rich chemistry of the ejecta. These abundances must be regarded as strict upper limits, since the distribution of H_2 in the Homunculus is unknown. In any case, these findings shed new light onto the peculiar molecular ecosystem of η Car, and establish its surroundings as a new laboratory to investigate the lifecycle of silicate dust in extreme astrophysical conditions.

Keywords: Massive stars (732) — Luminous blue variable stars (944) — Circumstellar matter (241) — Circumstellar dust (236) — Shocks (2086) — Astrochemistry (75)

1. INTRODUCTION

η Car is a massive binary system composed of a ~ 100 M$_\odot$ luminous blue variable (LBV), and a hotter, ~ 30 M$_\odot$ secondary with spectroscopic signatures typical of late-O and WR stars (Iping et al. 2005). The system is very eccentric (e = 0.9), with a well-determined orbital period of 5.54 years and a minimum separation at periastron of 1.5 A.U (Damineli 1996; Damineli et al. 2008). The primary, η Car A, is the archetypal member of the LBV family, and has captivated astronomers ever since it underwent a violent mass eruption in the 1840s (Frew 2004). This outburst, dubbed the "Great Eruption", released nearly 10^{50} erg (Smith et al. 2003; Smith 2013) –rivalling the energetic output of a SN–, and ripped off between 20 and 40 M$_\odot$ of stellar material (Morris et al. 2017). The heavily processed ejecta,

ashes of the CNO cycle, formed the Homunculus nebula (Gaviola 1950), a rapidly expanding ($v_{\rm exp} \sim 650$ km s^{-1}, Hillier & Allen 1992; Smith et al. 2018b) hourglass-shaped circumstellar structure with a current-day projected size of $\sim 0.18 \times 0.11$ pc. The Great Eruption was followed, almost 50 yr later, by a second, less energetic outburst (Smith & Frew 2011) that gave birth to an inner structure commonly referred to as the Little Homunculus (Ishibashi et al. 2003), mimicking a gigantic matryoshka doll. The exceptionally complex circumstellar environment produced by these successive events makes of η Car a unique testing ground to investigate (1) the nature of eruptive mass loss processes in massive stars near the Eddington limit (Smith et al. 2004; Smith & Morse 2019); and (2) the intricate wind interactions

in highly massive binary systems (Okazaki et al. 2008; Gull et al. 2009, 2016).

Located at 2350 pc from Earth (Smith 2006) toward the near side of the Carina arm, η Car and the Homunculus have been the target of multiple observing campaigns that, spreading across the entire electromagnetic spectrum, allowed for studying the central binary and its surroundings in great detail (see Davidson & Humphreys 2012 for a review). Spectroscopic observations of the circumstellar material have provided an accurate portrait of the atomic gas and dust in and around the Homunculus, unveiling a chemical panorama quite in line with other LBV nebulae, i.e., nitrogen-rich ejecta with a significant oxygen depletion (Davidson et al. 1982, 1986; Dufour et al. 1997; Smith & Morse 2004). However, due to the rather extreme conditions in the outskirts of η Car –hot temperatures, strong FUV fields–, only in the last two decades has the molecular content of the Homunculus begun to draw attention. The first detection of neutral gas was achieved by Smith & Davidson (2001), who reported H_2 $v = 1$ emission at 2.12 μm, tracing the surface of the Homunculus lobes. A few years later, high velocity absorption lines of CH and OH were identified through UV spectroscopy (Verner et al. 2005), and shortly after ammonia was reported toward the core region of the Homunculus (Smith et al. 2006). The first molecular survey was carried out by Loinard et al. (2012) with APEX, reporting six new species (CO, CN, HCO^+, HCN, HNC and N_2H^+) and two isotopologues (^{13}CO and $H^{13}CN$), thereby confirming η Car as the LBV with the richest molecular inventory.

Initial attempts to map the spatial distribution of this molecular material at high angular resolution with ATCA (HCN, Loinard et al. 2016) and ALMA (CO, Smith et al. 2018a) narrowed down the emission to the central few arcsec of the Homunculus. The gas, with a velocity dispersion of $\sim$300 km s^{-1}, has a kinematic age in good agreement with the Great Eruption, and follows the distribution of the equatorial structures of warm dust detected in mid-infrared observations (Morris et al. 1999), tracing a sort of equatorial ring or torus of radius $\sim$4400 AU. This ring, disrupted towards the NW –its near side, coincident with the projected direction of the orbit's major axis–, delineates the bright rims of the so-called "butterfly" nebula (Chesneau et al. 2005), a region of efficient dust processing where emission from several other species has been resolved, such as HCN or HCO^+ (Bordiu & Rizzo 2019, hereafter BR19). Interestingly, a thorough re-calibration of CO ALMA data by Zapata et al. (2022), significantly improving sensitivity, has revealed higher velocity components that may be

tracing the walls of the polar lobes of the Homunculus by means of limb brightening.

The most recent observations toward η Car with ALMA and Herschel continue enlarging its molecular inventory, reporting new detections of H_2O, CH_3OH (Morris et al. 2020) and multiple O-, C- and N-bearing species and reactive ions (Gull et al. 2020), many of them never detected before in a star of this kind. These findings unravel an unexpected molecular scenario for an early-type high-mass star in its final evolutionary stages. In this work, we analyse ALMA band 6 observations from the ALMAGAL program, with a resolution better than $\sim$0.4 arcsec, reporting the first detection of three Si-bearing molecules, namely SiO, SiS, and SiN, therefore adding yet another piece to the intriguing chemical puzzle of η Car. In Sect. 2 we describe the observations and data processing methods; in Sect. 3 we outline the findings of this work, putting them in a broader context and discussing their implications; and in Sect. 4 we summarize the results and lay out the next steps in this research.

2. OBSERVATIONS AND DATA REDUCTION

The ALMAGAL project (P.I: S. Molinari) is an ALMA Cycle 7 large program that aims at observing the 1 mm continuum and lines toward more than 1000 dense star forming clumps with $M > 500$ M$_\odot$ and $d < 7.5$ kpc. In the context of this program, the field ID 653755, centred on the coordinates $(\alpha, \delta) = (10h45'03.''27, -59°41'03.''74)$, was observed. The field serendipitously covers the position of η Car, located $\sim$2 arcsec East from the phase centre. Observations took place on April 4th, 2021, $\sim$one year after the last η Car's periastron passage (on 2020.2), using 44 antennas with a maximum baseline of 1.4 km, resulting in a synthesized beam of 0.38×0.31 arcsec (P.A.: 1.38°). The field was observed for 45 min, under good weather conditions (precipitable water vapour $\sim$ 2.95 mm).

The spectral setup consisted of four spectral windows, two wide windows covering the frequency ranges 217.00..218.87 and 219.08..220.95 GHz (spectral resolution $\sim$ 976.56 KHz), and two narrower, overlapping windows covering the ranges 218.08..218.55 and 220.38.220.85 (spectral resolution $\sim$ 244.14 KHz). Raw visibilities were calibrated and imaged employing CASA (v6.1.1.15) with the ALMA pipeline version 2020.1.0.40. The final products were a 2D continuum map at a reference frequency of 220 GHz, and four spectral cubes (one for each spectral window). We manually reprocessed the

products using the `SpectralCube`[1] Python library and the `GILDAS/CLASS`[2] software package. Despite the initial continuum subtraction performed on the visibilities before imaging, spectra toward the continuum-emitting region were found to have a highly structured baseline; this issue could be related to the amplification of small calibration systematics by the strong continuum of η Car (Abraham et al. 2022). To deal with this problem, we fitted and subtracted a 3rd order polynomial to the spectra in all positions. This method was able to remove a significant part of the spurious structure towards the central region, while keeping the baseline flat elsewhere. Finally, the data cubes were recentred on the J2000 coordinates of η Car, $(\alpha, \delta) = (10h45'03''.53, -59°41'04''.05)$.

In this work, we focus exclusively on the analysis of the cubes with the largest spectral coverage. Throughout the paper, we adopt the following conventions: (1) intensities are expressed in the original flux density scale of Jy beam^{-1}, unless explicitly noted otherwise; (2) velocities refer to the local standard of rest frame (LSR); and (3) positions are given as offsets from the coordinates of η Car.

3. RESULTS AND DISCUSSION

3.1. *Detections and identification*

After a careful inspection of the cubes, we identified emission from five molecules, namely SiO, SiS, SiN, ^{13}CO and ^{13}CN. To our knowledge, this constitutes the first detection of Si- and S- bearing compounds in the outskirts of η Car, and, in a wider context, in a highly evolved early-type massive star. Quantum numbers, lower level energies, and rest frequencies of the transitions detected are summarized in Table 1.

Table 1. List of molecules detected.

Species	Transition	$E_{\rm L}$ (cm^{-1})	ν_0 (GHz)
SiO	$J = 5 \to 4$	14.48	217.104
SiS	$J = 12 \to 11$	39.97	217.817
SiN	$N = 5 \to 4,\ J = 9/2 \to 7/2$	14.52	218.006
	$N = 5 \to 4,\ J = 11/2 \to 9/2$	14.59	218.512
^{13}CN	$N = 2 \to 1,\ J = 3/2 \to 1/2$	3.62	217.303
	$N = 2 \to 1,\ J = 5/2 \to 3/2$	3.65	217.467
^{13}CO	$J = 2 \to 1$	3.68	220.398

Silicon is an abundant element (solar abundance $n_{\rm Si}/n_{\rm H2} = 6.47 \times 10^{-5}$, Asplund et al. 2021), most of which is depleted on to dust, being mainly stored in grain cores and, to a lesser extent, in the mantles (Gusdorf et al. 2008). Shocks can destroy dust grains either via ion sputtering or, especially when propagating in a dense medium ($n_{\rm H_2} > 10^4$ cm^{-3}), via grain-grain collisions, effectively releasing Si back to gas phase (Schilke et al. 1997; Caselli et al. 1997; Guillet et al. 2009, 2011). For this reason, Si-bearing species like SiO are typically regarded as reliable tracers of shocked regions (Martin-Pintado et al. 1992). SiO and SiS have also been proposed as gas-phase precursors of silicate dust. In circumstellar envelopes of AGB stars, their fractional abundances have been observed to drop at a few stellar radii, possibly due to accretion onto dust grains (Lucas et al. 1992; Schöier et al. 2006, 2007; Wong et al. 2016).

The study of Si-bearing molecules is therefore crucial to understand the lifecycle of dust. Both SiO and SiS have been widely searched for in many astrophysical environments: SiO has been detected in molecular clouds (Wilson et al. 1971), envelopes of evolved stars of all chemical types (e.g. Morris et al. 1979; Bujarrabal et al. 1994; Schöier et al. 2006); star-forming regions (Lefloch et al. 1998; Jiménez-Serra et al. 2004); and even in the disk of the B[e] supergiant CPD-52 9243 (Kraus et al. 2015). Likewise, SiS has also been found in circumstellar envelopes of all chemical types (Grasshoff et al. 1981; Schöier et al. 2007; Danilovich et al. 2019; Massalkhi et al. 2019, 2020), star forming regions with outflows (Dickinson & Kuiper 1981; Ziurys 1988) and exceptionally, in L1157, a shocked region associated with a sun-like protostar (Podio et al. 2017). However, no detections have been achieved to date in the outskirts of a highly evolved, early-type massive star like η Car, where the physical conditions are in principle much less hospitable.

Contrary to SiO and SiS, SiN is a rather elusive molecule, that to date has only been found in three astrophysical environments: the C-rich envelope of IRC+10 216 (Turner 1992), the hot molecular core SgrB2(M) (Schilke et al. 2003), and the S-type AGB star W Aql (De Beck & Olofsson 2020).

Our line identification relies upon strong kinematic arguments, as only the SiO, SiS and SiN transitions listed in Table 1 match the observed velocities of CO, HCN and HCO$^+$ (BR19). Still, we assessed other alternative identifications to account for the complex kinematics of the circumstellar material. Several transitions of CH$_3$OH and SO$_2$ lie within 100 MHz of the rest frequencies of SiO and SiS (217.104 and 217.817 GHz, respectively). However, we find their corresponding velocities

to be largely incompatible with those of CO, HCN and HCO$^+$, in some cases off by more than $\sim$100 km s^{-1}. Moreover, the CH$_3$OH and SO$_2$ transitions have lower level energies ($E_{\rm L}$) in the range $\sim$500-2000 cm^{-1}, much higher than SiO and SiS, and also than the methanol transition detected by Morris et al. (2020). The excitation conditions required by such transitions are only achievable very close to the binary, where vibrationally excited HCN has been reported (BR19).

Similarly, we searched for other candidate lines to explain the features at 218.006 and 218.512 GHz that we attribute to SiN. Both SiN components lie close in frequency to the $10_{0,10} \rightarrow 9_{0,9}$ and $9_{2,7} \rightarrow 8_{2,6}$ transitions of ^{29}SiC$_2$ at 218.011 and 218.506 GHz. However, the non-detection of the $10_{0,10} \rightarrow 9_{0,9}$ transition of the presumably more abundant isotopologue SiC$_2$ at 220.773 GHz makes this identification highly unlikely, leaving SiN as the only plausible option.

3.2. *Spatial distribution and kinematics*

All the molecules trace a clumpy "C-shaped" structure, following the overall spatial distribution of the equatorial ring already seen in CO, HCN, H^{13}CN and HCO$^+$ (see fig. 1 in BR19). No molecular emission is detected in the direction of the star. Fig. 1 shows the peak intensity maps of SiO and ^{13}CO, the brightest lines in each band, divided by the corresponding rms maps. The resulting S/N maps highlight the genuine line emission, while removing spurious features toward the continuum-emitting region –where the noise is higher– that affected the original peak intensity maps. For convenience, we identified twelve significant emission clumps above 5σ in the SiO map. The clumps were labelled from A to L counter-clockwise starting from the North, as indicated in Fig. 1, and will henceforth serve as a positional reference.

The SiO clumps have an average projected distance to the star of $\sim$2 arcsec. Despite their similar distribution along the butterfly region, SiO and ^{13}CO are not perfectly correlated: closer inspection reveals an offset between emission peaks, especially pronounced in the SE/E clumps (the far side of the ring), the SiO being closer to η Car in projection by $\sim$0.1–0.2 arcsec ($\sim 275 - 550$ au). This offset, smaller than the beam, is genuine and was validated by checking against the CO $J = 3 \rightarrow 2$ data presented in BR19. It suggests that SiO may preferentially trace the inner rims of the butterfly nebula, more exposed to the fast wind of η Car, as proposed by Chesneau et al. (2005).

The spatial distribution of the other Si-bearing compounds is even more patchy, with reliable detections only in a subset of the clumps. SiS is detected towards clumps

C, D, E, F, G, H, J and L, whereas SiN is only found in positions D, F, G and H. In clump F, the two transitions at 218.006 and 218.512 GHz are detected at a $\sim$3σ level, whereas in the other clumps only the 218.512 GHz component is unambiguously found. Since the two transitions are expected to have similar line strengths, a relative difference could be explained either by noise fluctuations, or very localised non-LTE effects (as observed in NH$_3$ around G79.29+0.46, Rizzo et al. 2014).

In any case, the low S/N of most of these detections prevents us from producing meaningful maps of SiS and SiN, as the lines are only clearly resolved in averaged spectra. In this sense, the non-detection of SiS and SiN in clumps where SiO is present may either be a matter of sensitivity, or imply an actual chemical differentiation. Likewise, the overall clumpiness of Si-bearing species may be due to the limited sensitivity of the data, or indicate that only in certain places the right physical conditions for their formation are met in presence of sufficient Si. In view of the different relative intensities and radial offset between SiO and ^{13}CO, we are inclined to favour the second scenario.

The insets in Fig. 1 show the spectra of SiO and ^{13}CO, averaged in a circular aperture of radius 2.5 arcsec, centred on the star, that encompasses the main emission features. The two molecules show a similar overall profile, with most of the emission originating from the velocity range (-100, $+100$) km s^{-1}. We performed a Gaussian fitting, identifying three major kinematic components that explain the overall motion of the gas: blueshifted material towards the W/NW, the near side of the ring; redshifted gas towards the S/SE, the far side; and material towards the NE and SW moving at velocities relatively close to the systemic velocity of η Car (-19.7 km s^{-1}, Smith 2004). However, we note that the relative intensities of the components differ between SiO and ^{13}CO. In SiO, the redshifted component is the strongest, as clumps in the far side (e.g. E, F, G) are significantly brighter than the others. Such a difference may be a consequence of local density enhancements, or modulations intrinsic to the orbital phase.

Individual clumps, on the other hand, exhibit a more complex kinematic structure, with multiple velocity components spreading over several tens of km s^{-1}. This dispersion is more significant in the clumps located south of the star, possibly tracing turbulent or stratified gas. For the subsequent analysis, beam-averaged spectra were extracted in all the twelve positions. Full spectra are presented in Appendix A (Figs. 5 and 6). Fig. 2 shows the spectra of clump F, the brightest one in SiO, as a representative example, while Fig. 3 presents
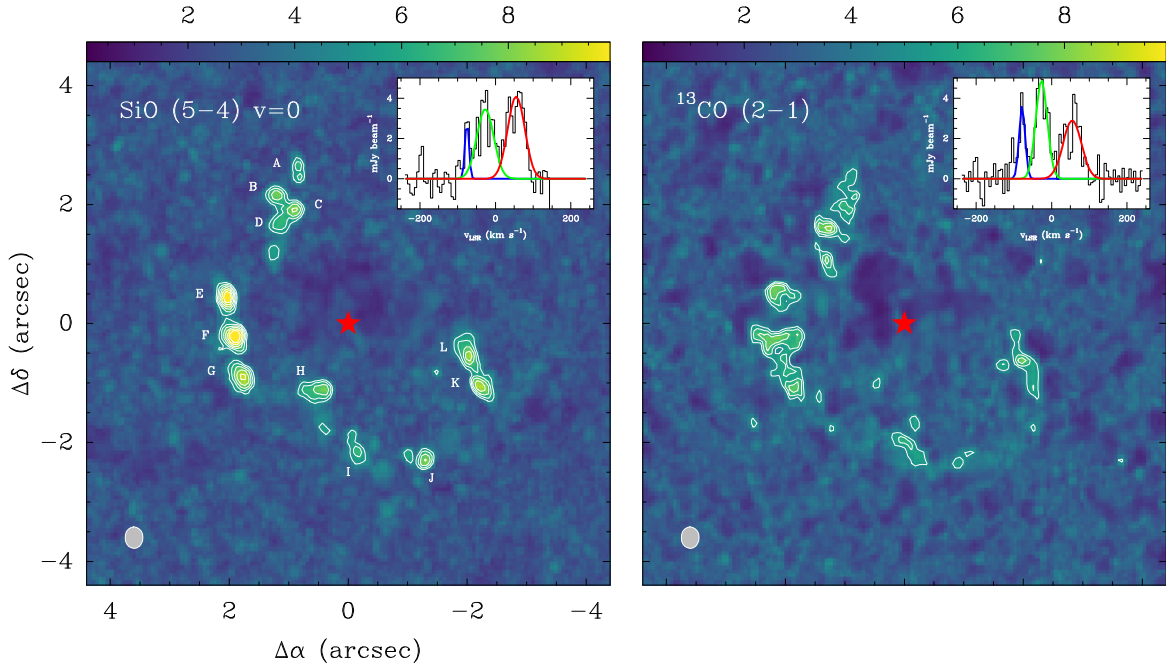
Figure 1. S/N maps of SiO $J = 5 \to 4$ ($v = 0$) and ^{13}CO $J = 2 \to 1$ towards η Car. Contours from 5 to 10. The position of η Car is indicated by the red marker. The approximate beam size is shown in the bottom-left corner. The insets show the average spectrum of each molecule, computed in a region of radius 2.5 arcsec. The dominant kinematic components are highlighted with Gaussian profiles. Since SiO appears next to the edge of the band, its spectrum is truncated above 140 km s^{-1}.

a closer view of the spectra of the Si-bearing molecules in that position, aligned in velocity.

3.3. Column densities

We employed the software `MADCUBA`[3] (Martín et al. 2019) to determine the column densities and molecular abundances of the observed species in all clumps. `MADCUBA` estimates the physical parameters of the emission by comparing the observed spectra with synthetic models computed under the only assumption of Local Thermodynamic Equilibrium (LTE). The AUTOFIT function of the `MADCUBA/SLIM` package (Spectral Line Identification and Modelling) performs a non-linear least-squares fit to the observed spectra, following the Levenberg-Marquardt algorithm (Levenberg 1944; Marquardt 1963), and returns the set of parameters (column density N, excitation temperature T_{ex}, line velocity and full width half maximum) that best reproduces the observed line profiles.

For the calculations, spectra were re-scaled to a main-beam temperature (T_{mb}) scale, using:

$$T_{\mathrm{mb}} = 1.222 \times 10^6 \frac{S_\nu}{\nu^2 \theta_{\mathrm{maj}} \theta_{\mathrm{min}}} \qquad (1)$$

---

[3] MAdrid Data CUBe Analysis (MADCUBA), developed at the Centro de Astrobiología. https://cab.inta-csic.es/madcuba/

with S_ν the flux density in Jy beam^{-1}, ν the reference frequency in GHz, and θ_{maj} and θ_{min} the major and minor axes of the beam in arcsec.

With just a single rotational transition observed in all the lines, the excitation temperature cannot be determined. We thus have proceeded under the assumption of thermal coupling between dust and gas, setting the T_{ex} of the clumps to the black-body equilibrium temperature of dust grains, as given by Smith et al. (2003),

$$T_{\mathrm{BB}} = 13100 \, R_{\mathrm{AU}}^{-1/2} \, \mathrm{K} \qquad (2)$$

where R_{AU} is the physical distance from each clump to η Car in AU, deprojected assuming an inclination of 41° (Smith 2006). This approach yields temperatures in the range 150–200 K, similar to those typically assumed in the literature. Finally, since all the clumps have a size comparable to the beam, we did not apply any filling factor correction.

Table 2 presents the column densities of SiO, SiS, SiN, ^{13}CO and ^{13}CN in the clumps, with their associated uncertainties. When a molecule is not detected, the 3σ upper limit of the column density is provided. As discussed in Sect. 3.2, some clumps show a complex kinematic structure, which results in multiple resolved velocity components. For those, the sum of independent column densities along the line of sight is provided. Line fitting parameters (observed velocity v, full width half maximum Δv, and integrated intensity) for all the com-
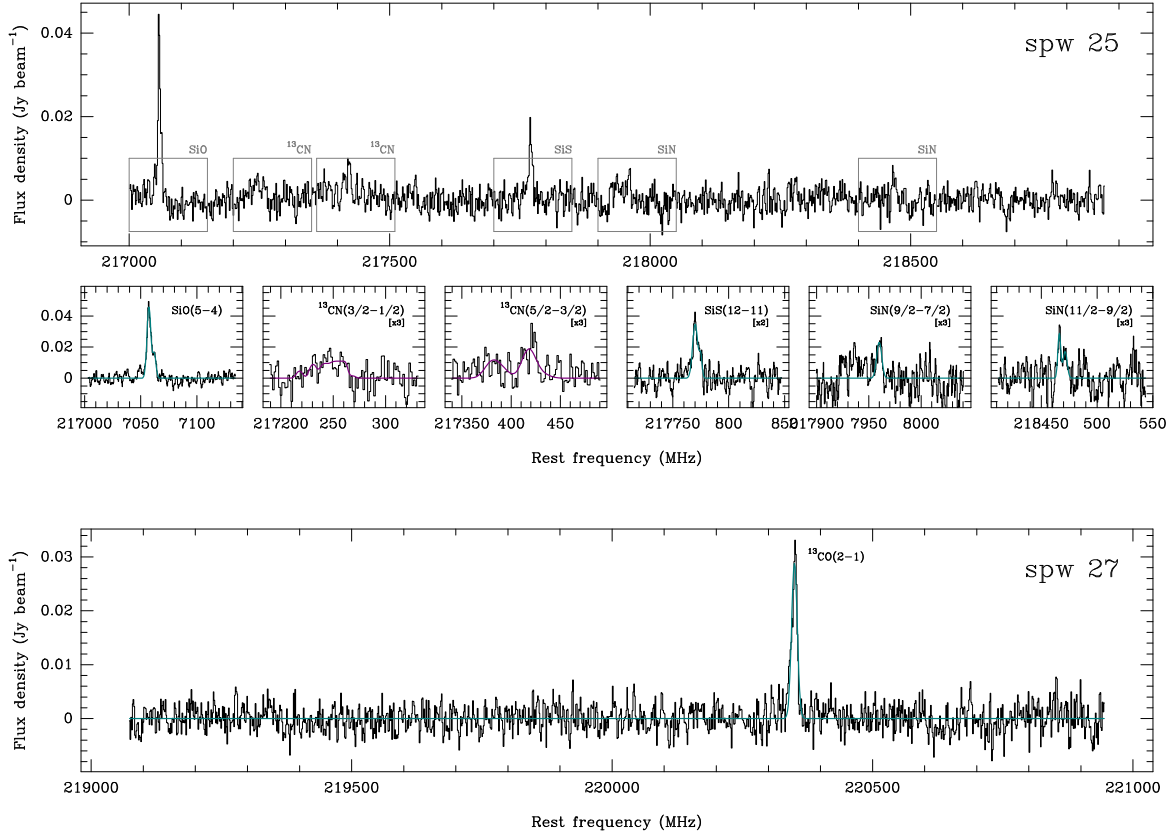
Figure 2. Beam-averaged spectra of clump F. Top panel: full band from 217.0 to 218.8 GHz, rebinned to a resolution of 2 km s^{-1}. The insets show zoom-ins of the transitions detected (grey boxes on the full spectrum) at the original resolution, with a gaussian (blue) or hyperfine (purple) fitting superimposed. The ^{13}CN spectra have been smoothed to better highlight the hyperfine structure. All the insets have the same flux density scale, with the different lines scaled appropriately for better visibility. Bottom panel: same as the top panel, from 219.1 to 221.0 GHz.

ponents with a signal-to-noise ratio above 3σ are listed in Appendix B (Tables 3 and 4).

We also checked for non-LTE effects using `RADEX` (van der Tak et al. 2007). `RADEX` solves the statistical equilibrium equations using the escape probability formulation (Sobolev 1960), without assuming LTE conditions. For the calculation, we set the H$_2$ volume density to 10^8 cm^{-3}, as suggested by Gull et al. (2020), the kinetic temperature to the temperatures in Table 2, and the column density to the values provided by `MADCUBA` for each component. Then, we compared the integrated line intensities observed with those predicted by `RADEX`. We found an average agreement better than 85% for SiO, better than 95% for SiS, and better than 97% for ^{13}CO. The slight discrepancy in SiO could perhaps be attributed to a possible weak maser contribution (see Sect. 3.6). In any case, considering the assumptions made, we conclude that non-LTE effects, while present, might not be particularly significant for the measured transitions.

All the lines are found to be optically thin, with τ in the range (0.01–0.1). When detected, the column densities range roughly from 0.7 to 3.5×10^{14} cm^{-2} for SiO, from 1.3 to 7.1×10^{14} cm^{-2} for SiS, and from 0.7 to 1.7×10^{15} cm^{-2} for SiN. We observe column density variations among clumps up to a factor of $\sim$5 in the case of SiO and SiS. Considering only the positions where the two species are detected (C, D, E, F, G, H, J and L), the [SiO/SiS] ratio has an average value of 0.6, meaning a slight overabundance of SiS over SiO. The clumps where SiS is not detected, namely A, B, I and K, have much higher ratios when considering the N(SiS) upper limits. Since the rms is similar across the clumps, the strong detections of SiO in absence of SiS in these positions may indicate a chemical differentiation. It is noteworthy that these clumps are among those located farthest from the star and hence with the lowest $T_{\rm ex}$. Contrarily, SiN is detected only towards four clumps (one of which is a tentative detection, see Table 3), showing the highest column density of the Si-bearing species. These clumps are not among those with the highest SiO and SiS col-

**Table 2.** Column densities of SiO, SiS, SiN, ^{13}CO and ^{13}CN in the positions indicated in Fig. 1.

Pos	$(\Delta\alpha, \Delta\delta)$	T_{ex}	N(SiO)	N(SiS)	N(SiN)	$N(^{13}$CO)	$N(^{13}$CN)
		(K)	$(\times 10^{14}$ cm$^{-2})$	$(\times 10^{14}$ cm$^{-2})$	$(\times 10^{14}$ cm$^{-2})$	$(\times 10^{17}$ cm$^{-2})$	$(\times 10^{15}$ cm$^{-2})$
A	$(+0.9, +2.6)$	154	0.74 (0.07)	< 0.64	< 1.46	0.69 (0.07)	< 0.14
B	$(+1.2, +2.2)$	166	1.53 (0.21)	< 0.51	< 1.51	1.19 (0.61)	< 0.15
C	$(+0.9, +1.9)$	180	1.42 (0.11)	2.25 (0.12)	< 1.65	1.34 (0.13)	< 0.42
D	$(+1.2, +1.7)$	185	1.39 (0.08)	2.19 (0.26)	7.11 (6.89)	2.61 (0.09)	0.88 (0.15)
E	$(+2.0, +0.4)$	179	1.79 (0.05)	3.38 (0.41)	< 1.62	1.76 (0.10)	0.73 (0.15)
F	$(+2.0, -0.2)$	173	2.75 (0.24)	4.83 (0.85)	17.38 (7.85)	2.44 (0.19)	0.92 (0.15)
G	$(+1.8, -0.9)$	163	2.51 (0.50)	3.38 (0.24)	7.46 (0.85)	1.74 (0.46)	< 0.42
H	$(+0.5, -1.1)$	211	3.51 (0.39)	7.05 (1.30)	< 2.69	2.89 (0.25)	1.17 (0.34)
I	$(-0.3, -2.2)$	165	2.90 (0.33)	< 0.40	< 1.58	3.45 (0.32)	< 0.25
J	$(-1.3, -2.3)$	162	1.33 (0.07)	3.56 (0.36)	< 1.54	3.19 (0.15)	< 0.17
K	$(-2.3, -1.1)$	168	2.04 (0.16)	< 0.53	< 2.02	2.40 (0.15)	1.34 (0.20)
L	$(-2.0, -0.5)$	180	1.66 (0.07)	1.30 (0.20)	< 2.20	2.25 (0.10)	1.34 (0.24)

NOTE—For clumps with multiple velocity components (see Tables 3 and 4), we provide the sum of column densities of individual components. When a line is not detected, we provide the 3σ upper limit of the column density.
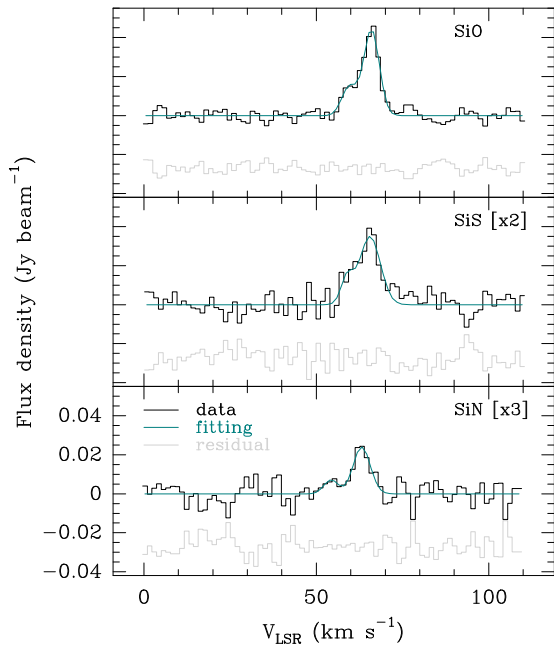
Figure 3. Velocity-aligned spectra of the Si-bearing molecules detected in clump F. The SiN transitions at 218.006 and 218.512 GHz have been stacked to improve signal-to-noise ratio. For each spectrum, a gaussian fitting (blue) and the corresponding residual (gray) are shown. The relative scaling of the lines is the same as in Fig. 2

umn densities, which could possibly imply a localised overabundance of SiN.

3.4. *Molecular abundances*

Translating column densities into molecular abundances is not straightforward in η Car, as the distribution of H$_2$ at angular scales comparable to the clumps is unknown. We are thus forced to adopt the global value
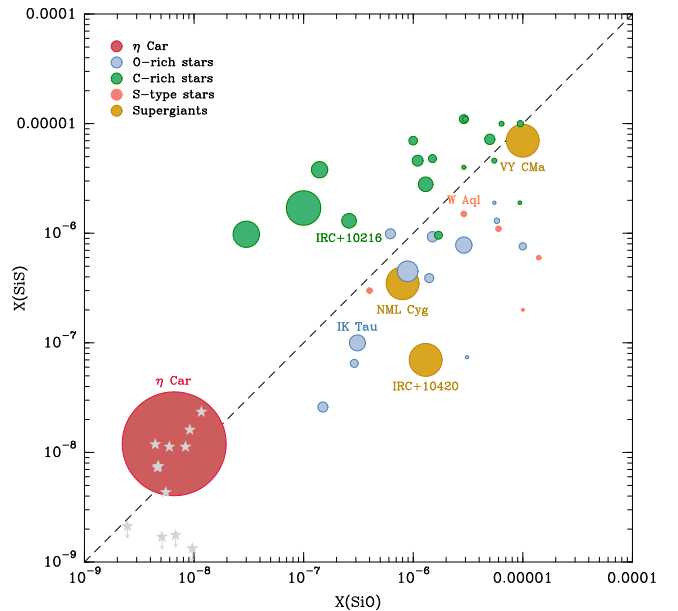
Figure 4. Comparison of abundances of SiO and SiS measured in η Car (this work) and other star types with confirmed detections of the two species: C-rich stars (Massalkhi et al. 2019), O-rich stars (Massalkhi et al. 2020), S-type stars (Ramstedt et al. 2009; Danilovich et al. 2018; De Beck & Olofsson 2020), the yellow hypergiant IRC+10420 (Quintana-Lacaci et al. 2016), and the red supergiants VY CMa (Ziurys et al. 2007) and NML Cyg (Singh et al. 2021). Some relevant objects have been labelled for clarity. The size of the markers is proportional to the square root of $\dot{M}$. The gray star markers around η Car indicate the abundances of individual clumps. The dashed line represents [SiO/SiS]= 1.

of $N(\mathrm{H}_2) = 3.0 \times 10^{22}$ cm^{-2} determined by Smith (2006). Taking average column densities for each molecule, considering only clumps with detections above 3σ, we de-

rive $[SiO/H_2] = 6.7 \times 10^{-9}$, $[SiS/H_2] = 1.2 \times 10^{-8}$ and $[SiN/H_2] = 3.6 \times 10^{-8}$. These values have to be regarded as peak abundances or upper limits, as we are assuming a homogeneous distribution of H_2, which may not reflect reality, i.e., it is likely that H_2 is somewhat enhanced in the clumps, resulting in lower abundances. Nevertheless, these values are a useful first estimate that allows us to put η Car in context with other evolved stars with a rich silicon chemistry.

Fig. 4 compares the SiO and SiS abundances of η Car with those measured in other sources, namely C-rich stars (Massalkhi et al. 2019), O-rich stars (Massalkhi et al. 2020), S-type stars (Ramstedt et al. 2009; Danilovich et al. 2018; De Beck & Olofsson 2020), the red supergiants VY CMa (Ziurys et al. 2007) and NML Cyg (Singh et al. 2021), and the yellow hypergiant IRC+10420 (Quintana-Lacaci et al. 2016). Only stars with confirmed detections of the two species have been included. We find that the abundances of η Car are exceptionally low, more than one order of magnitude lower than in other sources. This is in excellent agreement with the trend observed by González Delgado et al. (2003), who surveyed a large sample of AGB stars and found that the SiO fractional abundance and the mass-loss rate were inversely correlated regardless of the chemical type of the envelope, possibly as a consequence of enhanced depletion of SiO onto dust grains at higher densities. The case of SiS is particularly interesting. It is not detected in envelopes with $\dot{M} < 10^{-6}$ $M_\odot$ yr^{-1}, possibly due to a lack of available Si and S. Above this threshold, Massalkhi et al. (2019, 2020) found weak hints of an abundance decrease with increasing $\dot{M}$, similar to SiO, but only in C-rich envelopes. However, the abundances of η Car, with its extreme mass-loss rate of 10^{-3} $M_\odot$ yr^{-1} (Hillier et al. 2001), and other sources with mass-loss rates of a few $\sim 10^{-4}$ $M_\odot$ yr^{-1}, such as NML Cyg and IRC+10420, seem to support this trend. The only exception is VY CMa, which presents large abundances of SiO and SiS despite having a high mass-loss rate ($[SiO/H_2] = 10^{-5}$, $[SiS/H_2] = 7 \times 10^{-6}$, Ziurys et al. 2007).

Besides, in η Car, the clumps with detection of SiO and SiS have $[SiO/SiS] < 1$ (except for clump L), meaning that their silicon chemistry is somewhat closer to that of C-rich stars, where SiS tends to be more abundant than SiO by a factor of a few. Such an abundance ratio is not immediately explainable, considering: 1) the composition of the ejecta around η Car, which is rich in N but C- and O-poor; and 2) the lack of reported observations of sulphur-bearing species to explain the formation of SiS (see Sect. 3.5). In this respect, Zanchet et al. (2018) developed a simple shock model that predicts a slower post-shock formation of SiS than SiO, and with lower abundances. Still, we emphasize that η Car is an exceptional environment with rather unusual physical conditions, that probably will require the development of specific models to properly describe its molecular chemistry. In this context, a way to explain the prevalence of SiS over SiO follows the arguments presented by Massalkhi et al. (2019), who regard SiS as a more efficient gas-phase reservoir of Si, to the detriment of SiO, which is more easily incorporated back to dust grains as density and mass-loss rate increase. Indeed, condensation of SiO -and, to a lesser extent, of SiS– onto dust could be a recurring process in the molecular ring. The material in the inner rims of the butterfly region would be constantly recycled, with shocks caused by the binary winds periodically destroying dust and leading to the formation of Si-bearing species. A fraction of these molecules would eventually deplete back to dust, in a cycle modulated by the orbital period of 5.54 yr.

Finally, it is worth noting that photodissociation could also play an important role to explain the observed abundances. Unfortunately, its impact is difficult to calibrate: first, because the UV flux to which the circumstellar material is exposed is, again, a function of the orbital phase: depending on the epoch, a large fraction of the ionizing flux from the hotter secondary is blocked by the optically thick primary wind (Gull et al. 2016); and second, because the photodissociation rate of SiS is not yet well determined, and usually assumed similar to that of SiO (Massalkhi et al. 2019).

3.5. *Chemistry of Si-bearing molecules in the Homunculus*

The physics of dust formation in the massive winds and eruptions of hot evolved stars were studied by Kochanek (2011), who found that only extremely high mass-loss rates ($\dot{M} > 10^{-2.5}$ $M_\odot$ yr^{-1}) allowed for efficient condensation while providing sufficient self-shielding from UV radiation. In this context, the supply of gas-phase Si in η Car could be explained by looking at the impact of the fast winds of the central stars on the ejecta from the Great Eruption. In timescales of months/years, several solar masses of processed material were expelled, a fraction of which expanded in the equatorial plane of the system. This matter, dense and hot, eventually cooled down enough as to allow for the condensation of dust grains.

The dust content of the Homunculus at different spatial scales has been thoroughly studied by Morris et al. (1999) and Chesneau et al. (2005), who concluded that only a mix of silicates and corundum can account for the

spectral features observed in the infrared. This dust has been continuously exposed to the strong, optically thick primary wind ($v_{inf} \sim 420$ km s^{-1}), plus the intermittent impact of the much faster secondary wind ($v_{inf} \sim 3000$ km s^{-1}) modulated by the orbital cycle. The competing effect of these winds could possibly explain the processing of dust in the inner borders of the butterfly region, releasing Si back to gas phase (and explaining the radial offset observed between SiO and CO/^{13}CO emission reported in Sect. 3.2). We could also speculate about the differences in brightness of the SiO clumps resorting to the most accepted orbital geometry (e.g. Teodoro et al. 2016), which places the periastron on the far side of the orbit (i.e. "behind" η Car A, in the S/SE direction where SiO emission is more intense). This is also the dominant direction where receding, highly compressed fossil wind structures pile up (Gull et al. 2016) as a result of the fast dive of the secondary into the primary wind. The accumulated effect of such abrupt changes in the wind regime over several orbital cycles may favour the dust processing on the far side, hence explaining the observed brightness differences.

Chemical models addressing the formation and destruction of Si-bearing species predict two dominant formation routes for SiO, namely: (1) oxidation of gas-phase Si, primarily through Si + CO → SiO + C and Si + OH → SiO + H (Agúndez & Cernicharo 2006), and (2) reaction with sulphur-bearing compounds, via Si + SO → SiO + S, and Si + SO$_2$ → SiO + SO (Zanchet et al. 2018). The detection of CO (Loinard et al. 2012; Smith et al. 2018a) and OH in the Homunculus (Verner et al. 2005; Gull et al. 2020) may suggest that the former reactions are the preferential formation channels of SiO, whereas no other sulphur-bearing species –besides SiS, in this work– have been ever reported. In particular, SO$_2$, one of the main reservoirs of sulphur in AGB stars (Danilovich et al. 2016), has not yet been detected towards η Car. The ALMAGAL setup covers eight transitions of SO$_2$ spanning a wide range of E_L values ($\sim$200–3000 cm^{-1}), allowing us to set a 3σ upper limit column density $N(SO_2) < 10^{18}$ cm^{-2} following the assumptions in Sect. 3.3. This value, however, does not really set tight constraints, and still allows for a high fractional abundance. Finally, an alternate pathway for SiO formation involves the destruction of SiS through SiS + O → SiO + S. For this reaction to be dominant, sufficient free oxygen has to be available, which is unlikely in the environment of η Car, given that most of it should be already locked in CO, and other less abundant species like OH. However, it could explain an overabundance of SiO in the clumps where no SiS is detected.

Regarding SiS, the kinetics of chemical reactions leading to its formation are less understood. The primary paths involve reactions with SO and SO$_2$, competing with SiO but having lower reaction rate coefficients (Zanchet et al. 2018). As a consequence, the formation rate of SiO is always higher (by a factor of 5–7) than SiS. In a recent work, Mota et al. (2021) proposed an alternate gas-phase reaction, Si + SH → SiS + H, that was able to successfully explain the SiS overabundances observed in L1157 (Podio et al. 2017).

Follow-up observations specifically targeting other sulphur carriers will provide better insight on the feasibility of the different formation routes of SiO and SiS. We note, though, that most of the available chemical models address the conditions and abundances found in circumstellar envelopes or star forming regions, and hence may not be directly applicable to η Car, where conditions may differ by a large margin. The development of *ad hoc* models will surely be needed to explain the lifecycle of Si-bearing species in such a harsh, unusual ambient.

The formation of SiN is probably related to that of SiO and SiS. However, the current understanding of SiN gas-phase chemistry is limited. Provided that shocks supply enough Si, one of the main formation routes for SiN would be the neutral-neutral reaction (Roveri et al. 1988) Si + NH → SiN + H. In C-rich environments, another possible source of SiN could be a dissociative electron recombination following the reaction Si$^+$ + NH$_3$ → SiNH$_2^+$ + H (Turner 1992). In η Car, these two routes seem feasible, considering the recent detection of NH and NH$_3$ (Gull et al. 2020), a significant fraction of which may reside in the equatorial regions where SiN is found. Indeed, the high SiN abundance reflects the unusually nitrogen-rich chemistry of the Homunculus, consistent with heavily processed CNO ejecta.

3.6. *Is maser emission possible?*

The column densities and abundances derived in Sect 3.4 assume a thermal origin for the emission of all molecules. However, masers of SiO and its isotopologues have been frequently observed in envelopes of evolved stars (Schwartz et al. 1982; Pardo et al. 1998; Kim et al. 2010; Rizzo et al. 2021), even in their vibrational ground states ($v = 0$). SiS masers have been detected as well, but only in IRC+10216 (Henkel et al. 1983; Fonfría Expósito et al. 2006). One may wonder whether the maser scenario may also hold in η Car. In fact, SiO and SiS show some features that might be compatible with a maser contribution. First, SiO maser emission in evolved stars is generally clumpy, arising from discrete, very compact regions that usually trace a circumstellar ring due to tangential amplification (Colomer et al.

1992; Diamond et al. 1994, 1997); such a morphology resembles the spatial distribution of SiO around η Car, although at very different angular scales. Second, maser emission tends to show narrower velocity profiles than thermal emission; in our case, we observe that SiO and SiS have significantly narrower lines than ^{13}CO in many of the studied positions, as shown in Fig. 5.

The pumping mechanism of SiO masers is not completely established, with radiative and collisional pumping as the most plausible explanations. For these mechanisms to be effective, H_2 densities in excess of $\sim 10^9$ cm^{-3} and kinetic temperatures above 1000 K are required (Elitzur 1992; Bujarrabal 1994). Such stringent physical conditions are typically found at a few stellar radii from the stellar photosphere in the case of AGB stars, hence posing an important drawback for η Car, where material is located $\sim$ 5000 AU away from the binary. However, at this point there is no ground for rejecting the possibility that these conditions are locally met in unresolved, hot and dense pockets of gas. Any further assumption is mere speculation, as we cannot be certain about the nature of the SiO and SiS lines with just a single transition observed. Follow-up interferometric observations of higher J transitions and other vibrational states, will elucidate whether the observed emission is entirely thermal, or has a weak maser contribution.
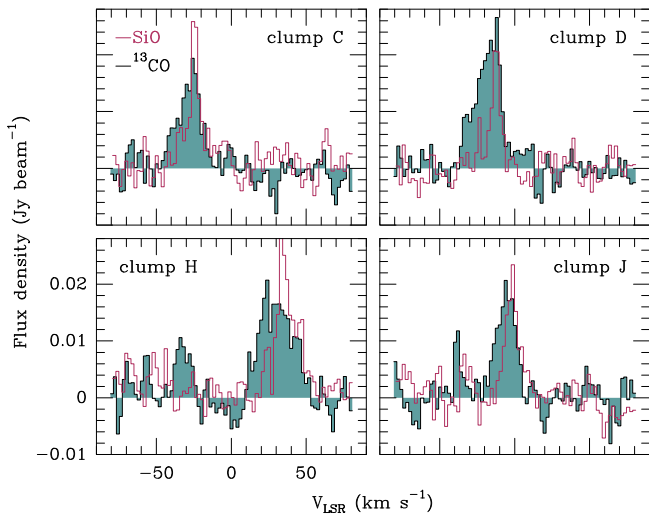

Figure 5. Comparison of the SiO and ^{13}CO line profiles in clumps C, D, H and J. Spectra have been smoothed to 2 km s^{-1}. All panels have the same intensity scale.

4. SUMMARY AND CONCLUSIONS

We have analysed ALMA band 6 observations toward η Car with a resolution better than 0.4 arcsec. We report the detection of SiO, SiS and SiN, the first Si-

and S-bearing species found in the outskirts of a highly evolved, early-type massive star. The molecules trace a clumpy equatorial ring that surrounds the central binary at a projected separation $\sim$2 arcsec, presumably dating back to the Great Eruption in the 19th century.

Considering the abrupt changes of the wind regime due to the binary interaction, we propose the continuous processing of dust grains in the inner rim of the butterfly region as the most likely source of the gas-phase silicon needed for the formation of these species. The recent detection of other molecules typically associated with shock-heated gas, like NH_3, CH_3OH, H_2O or CH^+ (Morris et al. 2020; Gull et al. 2020), even when their exact location in the Homunculus is yet to be pinpointed, may support this interpretation.

We have derived molecular abundances of [SiO/H_2] = 6.7×10^{-9}, [SiS/H_2] = 1.2×10^{-8}, and [SiN/H_2] = 3.6×10^{-8} in the clumps. The SiO and SiS abundances are significantly lower than those measured in AGB stars and cool supergiants, (1) making of η Car an outstanding object from the perspective of silicon chemistry, and (2) further confirming the trend of decreasing SiO and SiS abundances with increasing $\dot{M}$ inferred from observations of AGB stars. We suggest a more efficient re-adsorption of SiO into dust grains to explain the observed [SiO/SiS] ratio, whereas the prevalence of the rarer SiN over the other Si-bearing compounds seems consistent with the nitrogen-rich nature of the ejecta.

All in all, η Car gives us an unmatched opportunity to examine the lifecycle of dust and molecules in the outskirts of a hot, evolved star in affordable timescales. Further and deeper observations to complete its chemical inventory, along with new chemical models able to reproduce its time-dependent conditions, will provide an insightful view of the kinetic networks at work, contributing to fill the gaps in our knowledge about this fascinating object. Finally, we remark that a proper understanding of silicon chemistry in sources like η Car is also crucial to assess the relevance of early-type massive stars as factories of silicate dust, a role so far reserved to cooler objects and supernovae.

Data availability . The data presented in this work is publicly accessible from the ALMA archive. The NEANIAS project fully supports Open Science and encourages the application of FAIR principles. Therefore, we have exported the `MADCUBA` outputs in VO-compliant format (Rizzo et al. 2022) to ensure interoperability and reproducibility of the modelling results, making them available along with the processed spectra in the Zenodo repository at https://pending..upon..acceptance. The physical parameters are written as VOTables, and the resulting synthetic spectra as verified FITS files[4] compliant with the ObsCore data model[5].

REFERENCES

Abraham, Z., Beaklini, P. P. B., Cox, P., Falceta-Gonçalves, D., & Nyman, L.-Å. 2022, MNRAS, 517, 47, doi: 10.1093/mnras/stac2661

Agúndez, M., & Cernicharo, J. 2006, ApJ, 650, 374, doi: 10.1086/506313

Asplund, M., Amarsi, A. M., & Grevesse, N. 2021, A&A, 653, A141, doi: 10.1051/0004-6361/202140445

Bordiu, C., & Rizzo, J. R. 2019, MNRAS, 490, 1570, doi: 10.1093/mnras/stz2621

Bujarrabal, V. 1994, A&A, 285, 953

Bujarrabal, V., Fuente, A., & Omont, A. 1994, A&A, 285, 247

Caselli, P., Hartquist, T. W., & Havnes, O. 1997, A&A, 322, 296

Chesneau, O., Min, M., Herbst, T., et al. 2005, A&A, 435, 1043, doi: 10.1051/0004-6361:20041395

Colomer, F., Graham, D. A., Krichbaum, T. P., et al. 1992, A&A, 254, L17

Damineli, A. 1996, ApJL, 460, L49, doi: 10.1086/309961

Damineli, A., Hillier, D. J., Corcoran, M. F., et al. 2008, MNRAS, 384, 1649, doi: 10.1111/j.1365-2966.2007.12815.x

Danilovich, T., De Beck, E., Black, J. H., Olofsson, H., & Justtanont, K. 2016, A&A, 588, A119, doi: 10.1051/0004-6361/201527943

Danilovich, T., Ramstedt, S., Gobrecht, D., et al. 2018, A&A, 617, A132, doi: 10.1051/0004-6361/201833317

Danilovich, T., Richards, A. M. S., Karakas, A. I., et al. 2019, MNRAS, 484, 494, doi: 10.1093/mnras/stz002

Davidson, K., Dufour, R. J., Walborn, N. R., & Gull, T. R. 1986, ApJ, 305, 867, doi: 10.1086/164301

Davidson, K., & Humphreys, R. 2012, Eta Carinae and the Supernova Impostors, Astrophysics and Space Science Library (Springer New York). https://books.google.es/books?id=RXjAaThREPEC

Davidson, K., Walborn, N. R., & Gull, T. R. 1982, ApJL, 254, L47, doi: 10.1086/183754

De Beck, E., & Olofsson, H. 2020, A&A, 642, A20, doi: 10.1051/0004-6361/202038335

Diamond, P. J., Kemball, A. J., & Boboltz, D. A. 1997, Vistas in Astronomy, 41, 175, doi: 10.1016/S0083-6656(97)00028-7

Diamond, P. J., Kemball, A. J., Junor, W., et al. 1994, ApJL, 430, L61, doi: 10.1086/187438

Dickinson, D. F., & Kuiper, E. N. R. 1981, ApJ, 247, 112, doi: 10.1086/159015

Dufour, R. J., Glover, T. W., Hester, J. J., et al. 1997, in Astronomical Society of the Pacific Conference Series, Vol. 120, Luminous Blue Variables: Massive Stars in Transition, ed. A. Nota & H. Lamers, 255

Elitzur, M. 1992, Astronomical masers, Vol. 170, doi: 10.1007/978-94-011-2394-5

[4] https://cdsarc.cds.unistra.fr/vizier.submit/fitsvalidator.html
[5] https://www.ivoa.net/documents/ObsCore/

12

Fonfría Expósito, J. P., Agúndez, M., Tercero, B., Pardo, J. R., & Cernicharo, J. 2006, ApJL, 646, L127, doi: 10.1086/507104

Frew, D. J. 2004, Journal of Astronomical Data, 10, 6

Gaviola, E. 1950, ApJ, 111, 408, doi: 10.1086/145274

González Delgado, D., Olofsson, H., Kerschbaum, F., et al. 2003, A&A, 411, 123, doi: 10.1051/0004-6361:20031068

Grasshoff, M., Tiemann, E., & Henkel, C. 1981, A&A, 101, 238

Guillet, V., Jones, A. P., & Pineau Des Forêts, G. 2009, A&A, 497, 145, doi: 10.1051/0004-6361/200811115

Guillet, V., Pineau Des Forêts, G., & Jones, A. P. 2011, A&A, 527, A123, doi: 10.1051/0004-6361/201015973

Gull, T. R., Morris, P. W., Black, J. H., et al. 2020, MNRAS, 499, 5269, doi: 10.1093/mnras/staa3113

Gull, T. R., Nielsen, K. E., Corcoran, M. F., et al. 2009, MNRAS, 396, 1308, doi: 10.1111/j.1365-2966.2009.14854.x

Gull, T. R., Madura, T. I., Teodoro, M., et al. 2016, MNRAS, 462, 3196, doi: 10.1093/mnras/stw1829

Gusdorf, A., Cabrit, S., Flower, D. R., & Pineau Des Forêts, G. 2008, A&A, 482, 809, doi: 10.1051/0004-6361:20078900

Henkel, C., Matthews, H. E., & Morris, M. 1983, ApJ, 267, 184, doi: 10.1086/160857

Hillier, D. J., & Allen, D. A. 1992, A&A, 262, 153

Hillier, D. J., Davidson, K., Ishibashi, K., & Gull, T. 2001, ApJ, 553, 837, doi: 10.1086/320948

Iping, R. C., Sonneborn, G., Gull, T. R., Massa, D. L., & Hillier, D. J. 2005, ApJL, 633, L37, doi: 10.1086/498268

Ishibashi, K., Gull, T. R., Davidson, K., et al. 2003, AJ, 125, 3222, doi: 10.1086/375306

Jiménez-Serra, I., Martín-Pintado, J., Rodríguez-Franco, A., & Marcelino, N. 2004, ApJL, 603, L49, doi: 10.1086/382784

Kim, J., Cho, S.-H., Oh, C. S., & Byun, D.-Y. 2010, ApJS, 188, 209, doi: 10.1088/0067-0049/188/1/209

Kochanek, C. S. 2011, ApJ, 743, 73, doi: 10.1088/0004-637X/743/1/73

Kraus, M., Oksala, M. E., Cidale, L. S., et al. 2015, ApJL, 800, L20, doi: 10.1088/2041-8205/800/2/L20

Lefloch, B., Castets, A., Cernicharo, J., & Loinard, L. 1998, ApJL, 504, L109, doi: 10.1086/311581

Levenberg, K. 1944, Quarterly of Applied Mathematics, 2, 164

Loinard, L., Kamiński, T., Serra, P., et al. 2016, ApJ, 833, 48, doi: 10.3847/1538-4357/833/1/48

Loinard, L., Menten, K. M., Güsten, R., Zapata, L. A., & Rodríguez, L. F. 2012, ApJL, 749, L4, doi: 10.1088/2041-8205/749/1/L4

Lucas, R., Bujarrabal, V., Guilloteau, S., et al. 1992, A&A, 262, 491

Marquardt, D. W. 1963, SIAM Journal on Applied Mathematics, 11, 431, doi: 10.1137/0111030

Martín, S., Martín-Pintado, J., Blanco-Sánchez, C., et al. 2019, A&A, 631, A159, doi: 10.1051/0004-6361/201936144

Martin-Pintado, J., Bachiller, R., & Fuente, A. 1992, A&A, 254, 315

Massalkhi, S., Agúndez, M., & Cernicharo, J. 2019, A&A, 628, A62, doi: 10.1051/0004-6361/201935069

Massalkhi, S., Agúndez, M., Cernicharo, J., & Velilla-Prieto, L. 2020, A&A, 641, A57, doi: 10.1051/0004-6361/202037900

Morris, M., Redman, R., Reid, M. J., & Dickinson, D. F. 1979, ApJ, 229, 257, doi: 10.1086/156950

Morris, P. W., Gull, T. R., Hillier, D. J., et al. 2017, ApJ, 842, 79, doi: 10.3847/1538-4357/aa71b3

Morris, P. W., Waters, L. B. F. M., Barlow, M. J., et al. 1999, Nature, 402, 502, doi: 10.1038/990048

Morris, P. W., Charnley, S. B., Corcoran, M., et al. 2020, ApJL, 892, L23, doi: 10.3847/2041-8213/ab784a

Mota, V. C., Varandas, A. J. C., Mendoza, E., Wakelam, V., & Galvão, B. R. L. 2021, ApJ, 920, 37, doi: 10.3847/1538-4357/ac18c5

Okazaki, A. T., Owocki, S. P., Russell, C. M. P., & Corcoran, M. F. 2008, in Massive Stars as Cosmic Engines, ed. F. Bresolin, P. A. Crowther, & J. Puls, Vol. 250, 133–138, doi: 10.1017/S1743921308020413

Pardo, J. R., Cernicharo, J., Gonzalez-Alfonso, E., & Bujarrabal, V. 1998, A&A, 329, 219

Podio, L., Codella, C., Lefloch, B., et al. 2017, MNRAS, 470, L16, doi: 10.1093/mnrasl/slx068

Quintana-Lacaci, G., Agúndez, M., Cernicharo, J., et al. 2016, A&A, 592, A51, doi: 10.1051/0004-6361/201527688

Ramstedt, S., Schöier, F. L., & Olofsson, H. 2009, A&A, 499, 515, doi: 10.1051/0004-6361/200911730

Rizzo, J. R., Blanco, C., & Martin-Pintado, J. 2022, VIOMASS: Virtual Observatory Integration Of Madcuba And SLIM Spectra, Zenodo, doi: 10.5281/zenodo.7046117

Rizzo, J. R., Cernicharo, J., & García-Miró, C. 2021, ApJS, 253, 44, doi: 10.3847/1538-4365/abe469

Rizzo, J. R., Palau, A., Jiménez-Esteban, F., & Henkel, C. 2014, A&A, 564, A21, doi: 10.1051/0004-6361/201323170

Roveri, R. M., Erdelyi Mendes, M., & Singh, P. D. 1988, A&A, 199, 127

Schilke, P., Leurini, S., Menten, K. M., & Alcolea, J. 2003, A&A, 412, L15, doi: 10.1051/0004-6361:20031649

Schilke, P., Walmsley, C. M., Pineau des Forets, G., & Flower, D. R. 1997, A&A, 321, 293

Schöier, F. L., Bast, J., Olofsson, H., & Lindqvist, M. 2007, A&A, 473, 871, doi: 10.1051/0004-6361:20077887

Schöier, F. L., Olofsson, H., & Lundgren, A. A. 2006, A&A, 454, 247, doi: 10.1051/0004-6361:20054795

Schwartz, P. R., Zuckerman, B., & Bologna, J. M. 1982, ApJL, 256, L55, doi: 10.1086/183795

Singh, A. P., Edwards, J. L., Humphreys, R. M., & Ziurys, L. M. 2021, ApJL, 920, L38, doi: 10.3847/2041-8213/ac2c7c

Smith, N. 2004, MNRAS, 351, L15, doi: 10.1111/j.1365-2966.2004.07943.x

—. 2006, ApJ, 644, 1151, doi: 10.1086/503766

—. 2013, MNRAS, 429, 2366, doi: 10.1093/mnras/sts508

Smith, N., Brooks, K. J., Koribalski, B. S., & Bally, J. 2006, ApJL, 645, L41, doi: 10.1086/505934

Smith, N., & Davidson, K. 2001, ApJL, 551, L101, doi: 10.1086/319846

Smith, N., & Frew, D. J. 2011, MNRAS, 415, 2009, doi: 10.1111/j.1365-2966.2011.18993.x

Smith, N., Gehrz, R. D., Hinz, P. M., et al. 2003, AJ, 125, 1458, doi: 10.1086/346278

Smith, N., Ginsburg, A., & Bally, J. 2018a, MNRAS, 474, 4988, doi: 10.1093/mnras/stx3050

Smith, N., & Morse, J. A. 2004, ApJ, 605, 854, doi: 10.1086/382671

—. 2019, MNRAS, 489, 268, doi: 10.1093/mnras/stz1996

Smith, N., Morse, J. A., Gull, T. R., et al. 2004, ApJ, 605, 405, doi: 10.1086/382185

Smith, N., Andrews, J. E., Rest, A., et al. 2018b, MNRAS, 480, 1466, doi: 10.1093/mnras/sty1500

Sobolev, V. V. 1960, Moving Envelopes of Stars, doi: 10.4159/harvard.9780674864658

Teodoro, M., Damineli, A., Heathcote, B., et al. 2016, ApJ, 819, 131, doi: 10.3847/0004-637X/819/2/131

Turner, B. E. 1992, ApJL, 388, L35, doi: 10.1086/186324

van der Tak, F. F. S., Black, J. H., Schöier, F. L., Jansen, D. J., & van Dishoeck, E. F. 2007, A&A, 468, 627, doi: 10.1051/0004-6361:20066820

Verner, E., Bruhweiler, F., Nielsen, K. E., et al. 2005, ApJ, 629, 1034, doi: 10.1086/431917

Wilson, R. W., Penzias, A. A., Jefferts, K. B., Kutner, M., & Thaddeus, P. 1971, ApJL, 167, L97, doi: 10.1086/180769

Wong, K. T., Kamiński, T., Menten, K. M., & Wyrowski, F. 2016, A&A, 590, A127, doi: 10.1051/0004-6361/201527867

Zanchet, A., Roncero, O., Agúndez, M., & Cernicharo, J. 2018, ApJ, 862, 38, doi: 10.3847/1538-4357/aaccff

Zapata, L. A., Loinard, L., Fernández-López, M., et al. 2022, arXiv e-prints, arXiv:2205.13405. https://arxiv.org/abs/2205.13405

Ziurys, L. M. 1988, ApJ, 324, 544, doi: 10.1086/165914

Ziurys, L. M., Milam, S. N., Apponi, A. J., & Woolf, N. J. 2007, Nature, 447, 1094, doi: 10.1038/nature05905

APPENDIX

A. FULL SPECTRA

Figure 5. Beam-averaged spectra of η Car between 217.000 and 218.850 GHz extracted from the clumps indicated in Figure 1. Spectra have been smoothed to a resolution of ~ 5 km s^{-1}. In each panel, the markers indicate the frequencies of the transitions listed in Table 1, shifted to the velocity of the strongest SiO component.
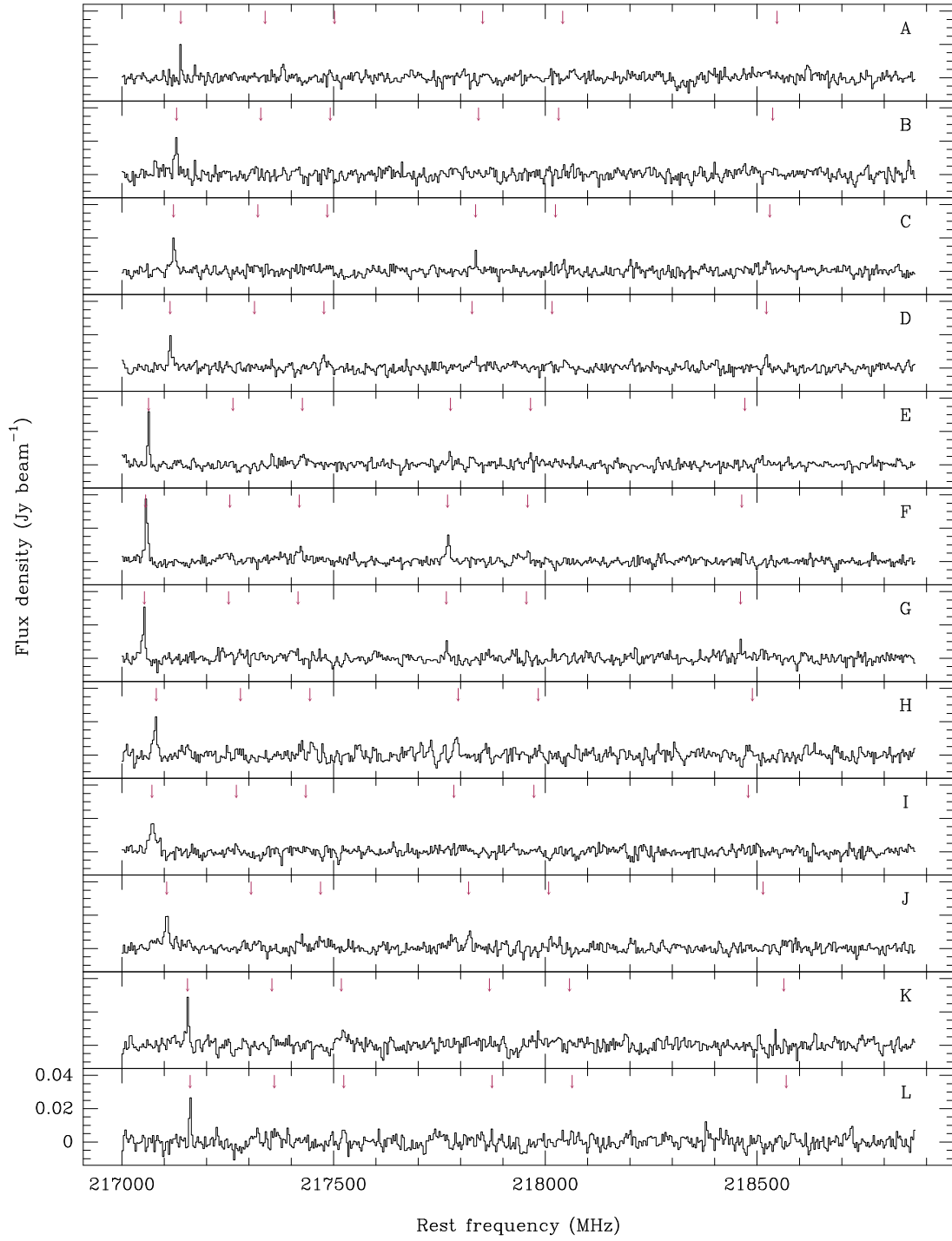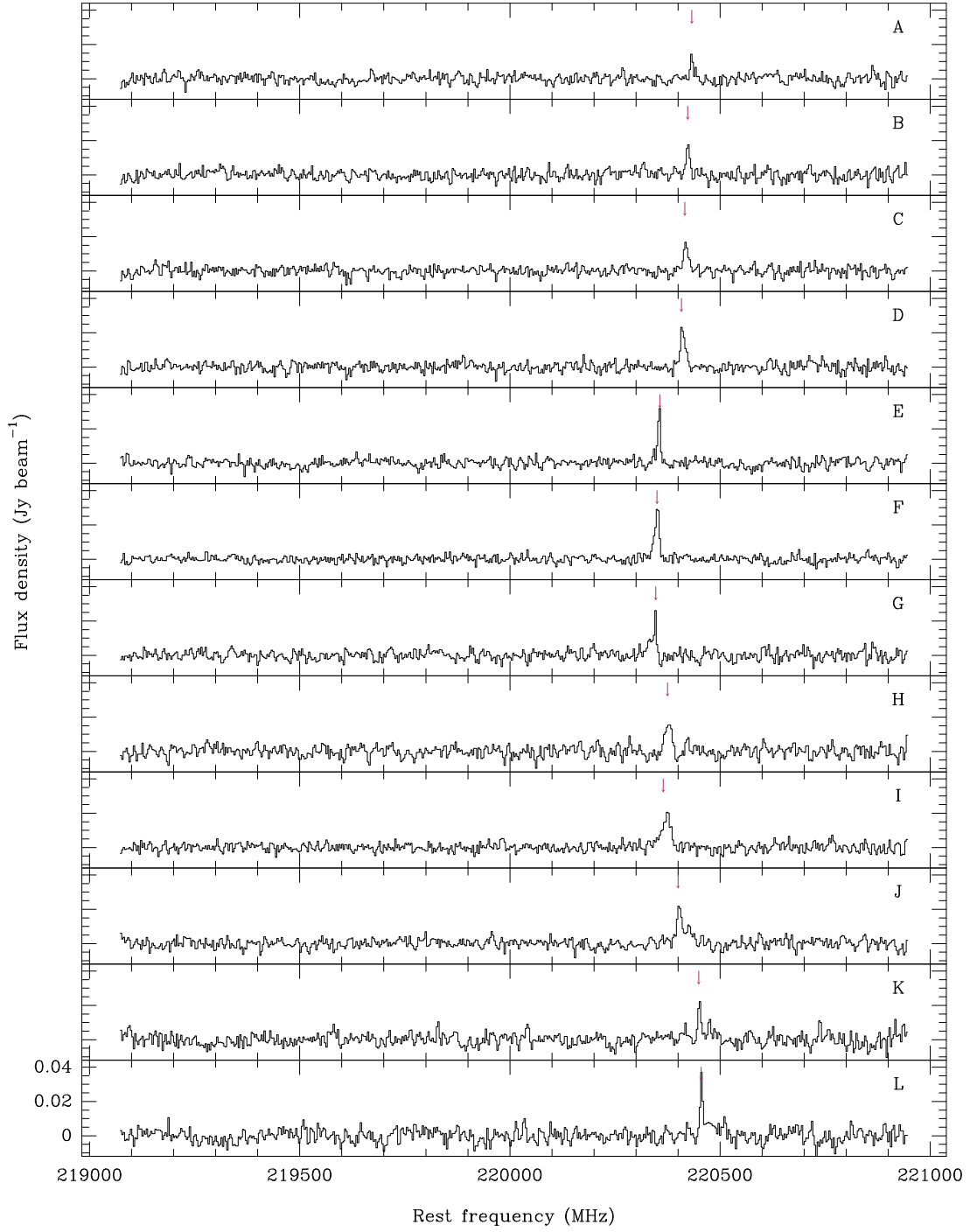
Figure 6. Beam-averaged spectra of η Car between 219.100 and 220.950 GHz, extracted from the clumps indicated in Figure 1. Spectra have been smoothed to a resolution of ~ 5 km s^{-1}. In each panel, the markers indicate the frequency of the ^{13}CO $J = 2 \rightarrow 1$ transition, shifted to the velocity of the strongest SiO component.

B. LINE FITTING

Table 3. `MADCUBA` line fitting parameters for SiO, SiS and SiN . Symbol # in the fourth column denotes component number, in order of increasing velocity.

Pos	$(\Delta\alpha, \Delta\delta)$	T_{ex}	#	SiO v_{LSR}	SiO Δv	SiO $\int T_{\mathrm{mb}}\delta v$	SiS v_{LSR}	SiS Δv	SiS $\int T_{\mathrm{mb}}\delta v$	SiN v_{LSR}	SiN Δv	SiN $\int T_{\mathrm{mb}}\delta v$
		(K)		(km s^{-1})	(km s^{-1})	(K km s^{-1})	(km s^{-1})	(km s^{-1})	(K km s^{-1})	(km s^{-1})	(km s^{-1})	(K km s^{-1})
A	$(+0.9, +2.6)$	154	1	-47.4	3.9 (0.4)	25.11 (2.43)	...	...	...	...	...	...
B	$(+1.2, +2.2)$	166	1	-33.5	5.4 (0.7)	34.16 (2.62)	...	...	...	...	...	...
			2	-25.4	7.1 (1.7)	15.09 (2.99)	...	...	...	...	...	...
C	$(+0.9, +1.9)$	180	1	-24.3	6.7 (0.6)	42.52 (3.33)	-24.9	4.4 (0.3)	17.36 (0.88)	...	...	...
D	$(+1.2, +1.7)$	185	1	-23.5	2.5 (0.4)	6.17 (0.91)	-24.4	5.5 (0.7)	10.72 (1.13)	...	...	...
			2	-12.4	6.4 (0.3)	34.66 (1.47)	-12.4	2.7 (0.4)	5.89 (0.79)	-14.3	4.2 (3.8)	3.88 (1.45)
E	$(+2.0, +0.4)$	179	1	57.8	5.9 (0.2)	53.86 (1.40)	58.0	8.6 (1.2)	26.13 (3.19)	...	...	...
F	$(+2.0, -0.2)$	173	1	59.2	4.8 (0.9)	19.35 (2.04)	60.0	6.0 (1.9)	14.49 (2.30)	56.6	10.0 (4.3)	5.84 (2.70)
			2	65.9	5.7 (0.4)	65.46 (2.21)	65.8	5.0 (1.0)	23.58 (2.11)	64.7	4.9 (2.0)	4.19 (1.88)
G	$(+1.8, -0.9)$	163	1	71.2	4.7 (0.5)	37.83 (1.98)	69.3	7.7 (0.6)	27.63 (1.99)	70.1	2.9 (0.8)	4.51 (1.32)
			2	78.4	13.7 (2.5)	43.98 (3.37)	...	...	...	...	...	...
H	$(+0.5, -1.1)$	211	1	23.6	3.8 (0.7)	9.94 (1.44)	...	...	...	...	...	...
			2	34.3	7.3 (0.6)	52.68 (2.00)	33.7	5.9 (1.0)	22.04 (1.65)	...	...	...
			3	40.4	2.9 (1.2)	7.08 (1.25)	39.5	4.0 (1.0)	12.94 (1.36)	...	...	...[a]
			4	45.9	6.3 (1.0)	23.08 (1.86)	44.9	5.0 (1.0)	14.05 (1.51)	...	...	...
I	$(-0.3, -2.2)$	165	1	44.0	31.0 (2.5)	82.44 (5.44)	...	...	...	...	...	...
			2	45.5	3.2 (1.8)	11.71 (1.75)	...	...	...	...	...	...
J	$(-1.3, -2.3)$	162	1	-5.7	5.8 (0.9)	16.68 (2.47)	-5.2	11.3 (1.4)	29.25 (2.76)	...	...	...
			2	-0.6	5.0 (1.0)	27.05 (2.29)	...	...	...	...	...	...
K	$(-2.3, -1.1)$	168	1	-76.1	2.5 (0.7)	4.96 (1.05)	...	...	...	...	...	...
			2	-70.0	5.5 (0.3)	45.99 (1.57)	...	...	...	...	...	...
			3	-61.0	5.3 (0.8)	13.75 (1.54)	...	...	...	...	...	...
L	$(-2.0, -0.5)$	180	1	-78.1	5.7 (0.3)	49.68 (2.20)	-76.5	3.5 (0.6)	10.03 (1.52)	...	...	...

NOTE—The fitting of SiN only considers the component at 218.512 GHz.

[a] Tentative detection at 2.5σ (see text).

Table 4. `MADCUBA` line fitting parameters for ^{13}CO and ^{13}CN . Symbol # in the fourth column denotes the component number, in order of increasing velocity.

				^{13}CO			^{13}CN		
Pos	$(\Delta\alpha, \Delta\delta)$	$T_{\rm ex}$	#	$v_{\rm LSR}$	Δv	$\int T_{\rm mb}\delta v$	$v_{\rm LSR}$	Δv	$\int T_{\rm mb}\delta v$
		(K)		(km s^{-1})	(km s^{-1})	(K km s^{-1})	(km s^{-1})	(km s^{-1})	(K km s^{-1})
A	(+0.9, +2.6)	154	1	−46.4	9.2 (1.0)	33.74 (3.21)	...	...	...
B	(+1.2, +2.2)	166	1	−43.0	2.7 (0.7)	5.98 (1.10)	...	...	...
			2	−38.4	3.4 (1.3)	6.74 (1.23)	...	...	...
			3	−33.3	8.8 (2.9)	38.02 (1.98)	...	...	...
			4	−23.8	3.7 (3.9)	3.84 (1.29)	...	...	...
C	(+0.9, +1.9)	180	1	−33.4	4.9 (0.0) ^{a}	11.13 (2.65)	...	...	...
			2	−25.2	10.9 (0.9)	46.22 (3.24)	...	...	...
D	(+1.2, +1.7)	185	1	−32.8	4.1 (1.1)	6.63 (1.75)	...	...	...
			2	−16.6	18.5 (0.8)	101.84 (3.72)	−12.8	13.5 (3.1)	0.01 (1.67)
E	(+2.0, +0.4)	179	1	57.9	6.1 (0.2)	51.37 (1.74)	58.2	13.5 (3.2)	0.01 (1.46)
			2	63.9	6.7 (0.8)	23.88 (2.43)	...	...	...
F	(+2.0, −0.2)	173	1	56.4	1.1 (0.9)	0.77 (0.40)	...	...	...
			2	64.5	11.4 (0.3)	91.38 (2.03)	62.3	10.4 (2.0)	0.01 (1.41)
			3	73.5	2.4 (0.0) ^{a}	7.89 (3.43)	...	...	...
			4	80.4	2.4 (0.0) ^{a}	7.33 (3.39)	...	...	...
G	(+1.8, −0.9)	163	1	71.1	5.6 (0.4)	38.45 (1.60)	...	...	...
			2	79.8	8.9 (4.7)	16.83 (2.01)	...	...	...
			3	91.9	13.0 (3.1)	26.09 (2.42)	...	...	...
H	(+0.5, −1.1)	211	1	12.2	1.8 (0.2)	3.84 (0.41)	...	...	...
			2	21.7	9.6 (0.7)	34.49 (2.31)	25.3	12.5 (6.1)	0.01 (2.16)
			3	31.7	7.8 (1.5)	10.68 (1.92)	...	...	...
			4	35.4	18.6 (1.4)	52.00 (3.36)	...	...	...
			5	44.7	4.3 (0.9)	6.18 (1.20)	...	...	...
I	(−0.3, −2.2)	165	1	19.3	6.5 (0.8)	17.61 (1.78)	...	...	...
			2	29.9	10.1 (0.6)	43.72 (2.29)	...	...	...
			3	40.3	18.3 (1.4)	44.90 (3.05)	...	...	...
			4	52.4	29.3 (4.1)	29.74 (3.79)	...	...	...
			5	70.0	47.0 (9.3)	23.84 (5.04)	...	...	...
J	(−1.3, −2.3)	162	1	−37.9	5.8 (0.0) ^{a}	25.12 (2.50)	...	...	...
			2	−6.7	24.7 (1.2)	124.21 (5.17)	...	...	...
K	(−2.3, −1.1)	168	1	−121.0	4.9 (0.8)	10.06 (1.44)	...	...	...
			2	−103.7	7.7 (0.6)	26.15 (1.80)	...	...	...
			3	−71.5	10.2 (0.4)	58.91 (2.07)	−76.4	14.1 (2.5)	0.02 (2.31)
			4	−26.5	5.6 (0.7)	13.96 (1.54)	...	...	...
L	(−2.0, −0.5)	180	1	−154.1	3.8 (0.5)	16.61 (1.76)	...	...	...
			2	−78.0	8.8 (0.3)	78.93 (2.68)	−79.3	13.3 (3.2)	0.02 (2.39)

^{a} The parameter had to be fixed to allow the fitting to converge simultaneously for all components.